



# Waste-Derived Copper-Lead Electrocatalysts for CO<sub>2</sub> Reduction

Shuang Yang,<sup>[a]</sup> Hongyu An,<sup>[a]</sup> Dimitra Anastasiadou,<sup>[b]</sup> Wenjie Xu,<sup>[c]</sup> Longfei Wu,<sup>[a]</sup> Hui Wang,<sup>[a]</sup> Jim de Ruiter,<sup>[a]</sup> Sven Arnouts,<sup>[d, e]</sup> Marta C. Figueiredo,<sup>[b]</sup> Sara Bals,<sup>[d]</sup> Thomas Altantzis,<sup>[e]</sup> Ward van der Stam,<sup>\*[a]</sup> and Bert M. Weckhuysen<sup>\*[a]</sup>

It remains a real challenge to control the selectivity of the electrocatalytic CO<sub>2</sub> reduction (eCO<sub>2</sub>R) reaction to valuable chemicals and fuels. Most of the electrocatalysts are made of non-renewable metal resources, which hampers their large-scale implementation. Here, we report the preparation of bimetallic copper-lead (CuPb) electrocatalysts from industrial metallurgical waste. The metal ions were extracted from the metallurgical waste through simple chemical treatment with ammonium chloride, and Cu<sub>x</sub>Pb<sub>y</sub> electrocatalysts with tunable compositions were fabricated through electrodeposition at varying cathodic potentials. X-ray spectroscopy techniques showed that the pristine electrocatalysts consist of Cu<sup>0</sup>, Cu<sup>1+</sup> and Pb<sup>2+</sup> domains, and no evidence for alloy formation was

found. We found a volcano-shape relationship between eCO<sub>2</sub>R selectivity toward two electron products, such as CO, and the elemental ratio of Cu and Pb. A maximum Faradaic efficiency towards CO was found for Cu<sub>9.00</sub>Pb<sub>1.00</sub>, which was four times higher than that of pure Cu, under the same electrocatalytic conditions. *In situ* Raman spectroscopy revealed that the optimal amount of Pb effectively improved the reducibility of the pristine Cu<sup>1+</sup> and Pb<sup>2+</sup> domains to metallic Cu and Pb, which boosted the selectivity towards CO by synergistic effects. This work provides a framework of thinking to design and tune the selectivity of bimetallic electrocatalysts for CO<sub>2</sub> reduction through valorization of metallurgical waste.

## Introduction

Capture and electrochemical conversion of carbon dioxide (CO<sub>2</sub>) to value-added products with renewably generated electricity is a promising strategy towards mitigation of the large scale emission of greenhouse gases into the atmosphere.<sup>[1,2]</sup> Copper (Cu) is a unique metal because of its moderate binding energy of crucial reaction intermediates, which enables Cu to produce both simple (*i. e.*, CO and HCOOH) and more complex reduction products (*i. e.*, C<sub>2+</sub> hydrocarbons and oxygenates) through electrocatalytic CO<sub>2</sub> reduction (eCO<sub>2</sub>R).<sup>[3,4]</sup> However, it is still a real challenge to direct and

control the selectivity of Cu for eCO<sub>2</sub>R, and an increase in the demand for Cu calls for alternative sources of this metal.<sup>[5–7]</sup> In this regard, using metal residues produced in the metallurgical industry as raw material to prepare electrocatalysts for CO<sub>2</sub> conversion, has gained researchers' attention recently.<sup>[8–11]</sup> Fayalite (Fe<sub>2</sub>(SiO<sub>4</sub>) mineral) slags, the residue from the Cu metallurgical industry, are rich in many potentially useful electrocatalytic elements, such as iron (Fe), zinc (Zn), copper (Cu), and lead (Pb) (Table S1). Compared to the traditional landfilling of these slags, which may change the original geological structures and worsen the quality of groundwater, unlocking the potential of this industrial waste to produce


[a] S. Yang, Dr. H. An, Dr. L. Wu, H. Wang, J. de Ruiter, Dr. W. van der Stam, Prof. B. M. Weckhuysen  
 Inorganic Chemistry and Catalysis  
 Debye Institute for Nanomaterials Science  
 Utrecht University  
 3584 CG Utrecht (The Netherlands)  
 E-mail: w.vanderstam@uu.nl  
 b.m.weckhuysen@uu.nl  
 Homepage: <https://inorganic-chemistry-and-catalysis.eu/thestaff/ward-van-der-stam/>  
<https://inorganic-chemistry-and-catalysis.eu/thestaff/b-m-weckhuysen/>


[b] D. Anastasiadou, Dr. M. C. Figueiredo  
 Laboratory of Inorganic Materials and Catalysis  
 Department of Chemical Engineering and Chemistry  
 Eindhoven University of Technology  
 5600 MB Eindhoven (The Netherlands)


[c] W. Xu  
 National Synchrotron Radiation Laboratory  
 CAS Center for Excellence in Nanoscience  
 University of Science and Technology of China  
 Hefei 230029 (P. R. China)

[d] S. Arnouts, Prof. S. Bals  
 Electron Microscopy for Materials Science (EMAT)  
 University of Antwerp  
 2020 Antwerp (Belgium)

[e] S. Arnouts, Prof. T. Altantzis  
 Applied Electrochemistry and Catalysis (ELCAT)  
 University of Antwerp  
 Antwerpen, 2610 Wilrijk (Belgium)

 Supporting information for this article is available on the WWW under <https://doi.org/10.1002/cctc.202200754>

 This publication is part of a joint Special Collection with EurJOC and EurJIC on the Netherlands Institute for Catalysis Research. Please see our homepage for more articles in the collection.

 © 2022 The Authors. ChemCatChem published by Wiley-VCH GmbH. This is an open access article under the terms of the Creative Commons Attribution Non-Commercial License, which permits use, distribution and reproduction in any medium, provided the original work is properly cited and is not used for commercial purposes.

catalytic materials that selectively convert CO<sub>2</sub> into valuable chemicals has the potential to create a self-sustainable cycle of critical elements.<sup>[12–15]</sup>

A promising approach to improve the electrocatalytic selectivity of Cu for eCO<sub>2</sub>R is the utilization of bimetallic systems.<sup>[16–20]</sup> Many reports have demonstrated that the binding strength of specific intermediates on the bimetallic catalyst surface could be rationally modified based on the relative oxygen (O) and hydrogen (H) affinities of the two metals.<sup>[9]</sup> Post-transition metals, such as tin (Sn), bismuth (Bi), lead (Pb) and indium (In), are known to have weak H binding and strong O binding, which resulted in excellent abilities to suppress the competitive hydrogen evolution reaction (HER) in eCO<sub>2</sub>R.<sup>[21–24]</sup> Bimetallic Cu-based catalysts including post-transition metals, such as copper/indium, copper/tin and copper/bismuth, have been recently reported to boost the selectivity for C<sub>1</sub> products at moderate current density.<sup>[25–27]</sup> Furthermore, it is known that product selectivity in a Cu-based bimetallic system is highly sensitive to the composition of the catalysts, and variations in metal ratios can lead to an enhanced selectivity for specific products.<sup>[28–33]</sup> Tuning the structure and composition of electrocatalysts therefore constitutes an attractive strategy to improve the selectivity of eCO<sub>2</sub>R catalysts.

In this work, we have fabricated a series of Cu<sub>x</sub>Pb<sub>y</sub> (x + y = 10) electrocatalysts with tunable compositions directly from industrial metallurgical waste through chemical extraction and electrodeposition at varying potentials, and deployed them in eCO<sub>2</sub>R. The morphology and structure of the Cu<sub>x</sub>Pb<sub>y</sub> electrocatalysts were identified by Scanning Electron Microscopy (SEM), high-resolution High Angle Annular Dark Field Scanning Transmission Electron Microscopy (HAADF-STEM), X-ray Photoelectron Spectroscopy (XPS), X-ray Diffraction (XRD) and X-ray Absorption Spectroscopy (XAS), which indicate that the pristine Cu<sub>x</sub>Pb<sub>y</sub> electrocatalysts are phase-separated structures with Cu<sup>0</sup>, Cu<sup>1+</sup> and Pb<sup>2+</sup> domains. The electrocatalytic performance showed that the selectivity towards CO could be tuned by varying the amount of Pb and the maximum Faradaic efficiency (41.1% CO at –1.05 V vs. RHE) was found for Cu<sub>9.00</sub>Pb<sub>1.00</sub> in 0.1 M KHCO<sub>3</sub> aqueous solution, which was four times higher than that of pure Cu (9.7% CO at –1.05 V vs. RHE) under the same electrochemical conditions. We found that the Cu<sup>1+</sup> and Pb<sup>2+</sup> domains were reduced *in situ* to their active metallic counterparts, as evidenced by *in situ* Raman spectroscopy and *ex situ* XRD measurements, and that the reducibility of the metal species was influenced by the electrocatalyst composition. These results suggest that there is a synergy between electrochemically reduced Cu and Pb, which tunes the reaction pathway to CO formation. Our study provides a new understanding of synergistic effects in Cu-based bimetallic system for eCO<sub>2</sub>R and constructs a framework for rational design of bimetallic electrocatalysts from industrial waste.

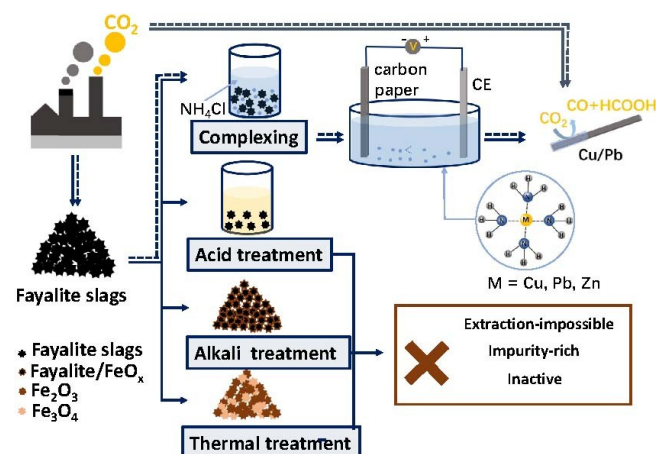
## Results and Discussion

As the main solid residue from the metallurgical industry, fayalite slags (supplier: Aurubis Beerse NV) are composed of

irregular particles with diameters from 0.50 cm to 1.00 cm (Figure S1). Their main crystal structure is found to be fayalite (Fe<sub>2</sub>(SiO<sub>4</sub>) mineral), as evidenced by X-Ray Diffraction (XRD) measurements (Figure S2), in which over twenty different elements co-exist as analyzed with Inductively Coupled Plasma-Optical Emission Spectrometry (ICP-OES, Table S1). Due to their complicated composition and high chemical resistance, degradation in a natural environment and direct reuse of the fayalite slags are difficult to achieve. To find the most effective extraction strategy, we have performed different treatments to the fayalite slags and compared their feasibility for metal ion extraction, as shown in Scheme 1.

Most commonly employed extraction techniques were first conducted to fayalite slags, including acid treatment, alkali treatment and thermal treatment. It was found that neither the use of acid or alkali was capable of further processing the fayalite slags due to the passivation and the residual impurities, which makes the separation and extraction impossible (see more details in Supporting Information, SI). Thermal treatment successfully changed the fayalite slags into iron oxide and SiO<sub>2</sub> (Figure S6), but still kept most impurities inside. In contrast to the above-mentioned treatments, complexing with ammonium chloride (NH<sub>4</sub>Cl) presents a more facile, sustainable and safer way to reuse this industrial residue. By complexing with NH<sub>3</sub> and Cl<sup>–</sup>, certain elements could be selectively extracted from the fayalite slags (such as copper (Cu), lead (Pb) and zinc (Zn), as shown in Table S2). With the subsequent electrodeposition, we managed to fabricate the electrocatalysts with controllable composition and structure.

As illustrated in Scheme 1, the metal elements were extracted from the fayalite slags by mixing with concentrated NH<sub>4</sub>Cl aqueous solution. The Cu<sup>2+</sup> and Pb<sup>2+</sup> cations from the fayalite slags could form stable complexes with NH<sub>3</sub> and Cl<sup>–</sup> ([Cu/Pb (NH<sub>3</sub>)<sub>4</sub>]<sup>2+</sup> and [CuCl<sub>4</sub>]<sup>2–</sup>) after one day of stirring at room temperature (see Figure S7 for the corresponding UV-vis spectra).<sup>[34,35]</sup> The resulting solution was filtrated to remove undissolved species and the obtained filtrate was subsequently



**Scheme 1.** Comparison of different residue treatments and the preparation of waste-derived copper-lead bimetallic electrocatalysts through chemical extraction and electrodeposition, as described in this work.

transferred into a one-cell electroplating bath to fabricate the working electrode for eCO<sub>2</sub>R catalysis. Different potentials (−0.6 V to −1.4 V with steps of −0.2 V, potentials are given vs. Ag/AgCl) were used during electrodeposition in order to tune the electrocatalyst composition. For comparison, Cu-1 and Pb-1 were also prepared from commercial highly purified Cu- and Pb-salts by electrodeposition under similar conditions (SI).

The elemental ratio of the pristine electrocatalysts was studied by ICP-OES (Table S3). From this analysis, it is evident that Cu dominates in all samples, but Pb is incorporated from −0.6 V vs. Ag/AgCl onward. The Pb content regularly increases with increasing applied cathodic bias until −1.2 V vs. Ag/AgCl, at which zinc and nickel start to appear. The XRD measurements (Figure S8) confirm the formation of a metallic Cu fcc phase, in which dominant Cu(111) and Cu(200) reflections can be discerned. We also observe the XRD reflections of Cu<sub>2</sub>O in Cu<sub>9.00</sub>Pb<sub>1.00</sub>, Cu<sub>8.65</sub>Pb<sub>1.65</sub> and Cu-1, which can be attributed to the inevitable oxidation of the copper surface due to air exposure, contact with the aqueous electrolyte, or the strong oxygen evolution at the anode under high applied bias during electrodeposition. However, no reflections from Pb or Pb-containing

compounds (e.g., PbO) were found, which might be due to their relatively low content, poor crystallinity or small crystalline domain size. Furthermore, no shifts of Cu reflections are observed, which indicates that pure Cu phases are formed, and no alloy formation with Pb occurred.

The local morphological structure and chemical composition of the pristine bimetallic electrocatalysts were investigated using SEM, high-resolution High Angle Annular Dark Field Scanning Transmission Electron Microscopy (HAADF-STEM) and STEM Energy Dispersive X-ray spectroscopy (STEM-EDS) measurements, as shown in Figure 1 and Figures S9–12. Cu<sub>9.20</sub>Pb<sub>0.80</sub> shows the particle-like structure in which small particles aggregate together to form larger particles. Cu<sub>9.00</sub>Pb<sub>1.00</sub> has dendrite-like structure, which is also composed of small particles. It was found that Cu<sub>9.20</sub>Pb<sub>0.80</sub> has a larger particle size (100–200 nm, Figure S9) compared to Cu<sub>9.00</sub>Pb<sub>1.00</sub>, in which a uniform distribution of particles with sizes ranging between 30 and 50 nm was observed (Figure 1a and Figure S10). From the high resolution HAADF-STEM data and the corresponding Fourier Transforms (FTs) (Figure 1b) together with the STEM-EDS mapping (Figures S11), it can be clearly observed that Cu,

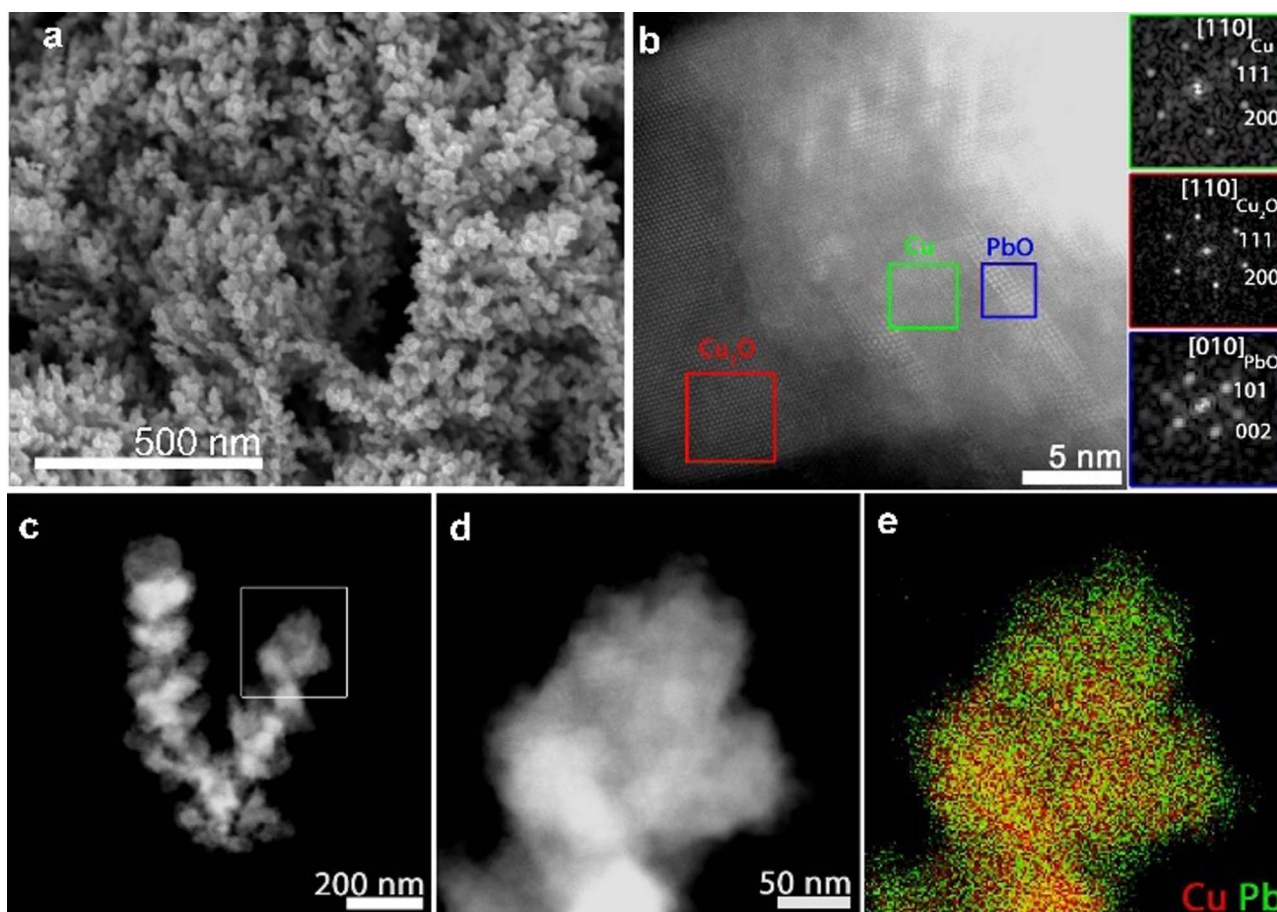


**Figure 1.** (a) Scanning Electron Microscopy (SEM) image of the Cu<sub>9.00</sub>Pb<sub>1.00</sub> electrode, indicating a particle size of 30 to 50 nm. (b) High-resolution High Angle Annular Dark Field Scanning Transmission Electron Microscopy (HAADF-STEM) image of Cu<sub>9.00</sub>Pb<sub>1.00</sub> together with the corresponding FTs (insets) from the regions indicated by squares of different color, clearly revealing crystalline Cu, Cu<sub>2</sub>O and PbO domains. (c) Overview HAADF-STEM image, (d) magnified HAADF-STEM image of the region indicated by the white rectangle in (c), together with (e) the corresponding Energy Dispersive X-ray spectroscopy (EDS) map of the Cu<sub>9.00</sub>Pb<sub>1.00</sub> sample.

Cu<sub>2</sub>O and PbO are present in the Cu<sub>9,00</sub>Pb<sub>1,00</sub> sample. We also found a very small fraction of regions in which the lattice fringes correspond to metallic Pb (Figure S12). The HAADF-STEM measurements (Figure 1c) and the related STEM-EDS mapping (Figure 1d, e) confirm the homogeneous distribution of Cu and Pb, suggesting that Pb species do not form individual nanoparticles. Cu<sub>8,65</sub>Pb<sub>1,35</sub> also shows a dendrite-like shape, while two distinct types of structures are observed, namely nanoparticles and nanorods. SEM-EDS experiments (Figures S13 and S14) suggest that the increased amount of Pb resulted in aggregation of Pb into nanorods.<sup>[36]</sup> The thickness of the studied catalysts was determined by Atomic Force Microscopy (AFM, Figure S15–S17). The thickness of the catalyst layer on carbon paper substrate was determined to be 2.5 μm, 1.5 μm and 1.1 μm in Cu<sub>9,20</sub>Pb<sub>1,0</sub>, Cu<sub>9,00</sub>Pb<sub>1,00</sub> and Cu<sub>8,65</sub>Pb<sub>1,35</sub>, respectively.

To gain insight into the chemical state of the surface of the pristine electrocatalysts, X-ray Photoelectron Spectroscopy (XPS) measurements were performed. Table S4 shows the atomic ratio of Cu and Pb at the surface, as determined by XPS measurements. Compared with the ratios obtained by ICP-OES, the Pb/Cu ratio is found to be quite similar, showing that Pb is homogeneously distributed throughout the electrodeposited catalyst. Small variations could be caused by the different surface morphologies of the prepared catalysts. As shown in Figure 2a, the Cu 2p<sub>3/2</sub> XPS spectra were deconvoluted into peaks at 932.6 eV and 934.6 eV, corresponding to Cu<sup>0/+</sup> and Cu<sup>2+</sup>, respectively.<sup>[37–39]</sup> For all samples, a higher contribution of Cu<sup>1+</sup> was observed from Cu LMM spectra than Cu<sup>0</sup> (Figure S18), which indicates that the surface of Cu-based electrocatalysts is

prone to surface oxidation. This is consistent with the XRD results, in which reflections of Cu<sub>2</sub>O were observed in all cases. The XPS Pb 4f spectra (Figure 2b) show the domination of Pb<sup>2+</sup> species on the surface of all measured samples, as evidenced by the binding energy of the Pb 4f electrons, along with a negligibly small peak of metallic Pb (136.5 eV) observed in the XPS measurements, consistent with the high resolution HAADF-STEM data.<sup>[40,41]</sup> The representative O 1s spectrum (Figure S19) showed three types of O species, which are identified as metal-oxygen (530 eV) bond, carbon-oxygen (531.4 eV) bond and oxygen-hydrogen bond (534.0 eV) respectively.<sup>[42,43]</sup> Taken together, it is evident that both Cu and Pb have been oxidized on the surface. This might be caused by inevitable air exposure of these two metals during the preparation by electrodeposition, or due to the aqueous electrolyte solution that was used for the electrocatalyst preparation.<sup>[44]</sup>

The local structure and the electronic nature of the pristine electrocatalysts were determined by X-Ray Absorption Spectroscopy (XAS), including X-Ray Absorption Near Edge Spectroscopy (XANES) and Extended X-Ray Absorption Fine Structure (EXAFS) measurements. In Figure 2c, the Cu K-edge XANES spectrum of Cu<sub>9,00</sub>Pb<sub>1,00</sub> displays a similar shape as that of Cu foil and Cu-1, indicating that these samples have similar structures.<sup>[45]</sup> Their identical Cu–K edge positions in XANES reveal that the bulk oxidation state of Cu in Cu<sub>9,00</sub>Pb<sub>1,00</sub> is close to the metallic Cu<sup>0</sup> phase. From the Fourier-transformed k<sup>3</sup>-weighted EXAFS spectra (Figure 2d and Figure S21a), the main characteristic peaks are found to be Cu–Cu scattering for these three samples, indicating the predominant existence of metallic

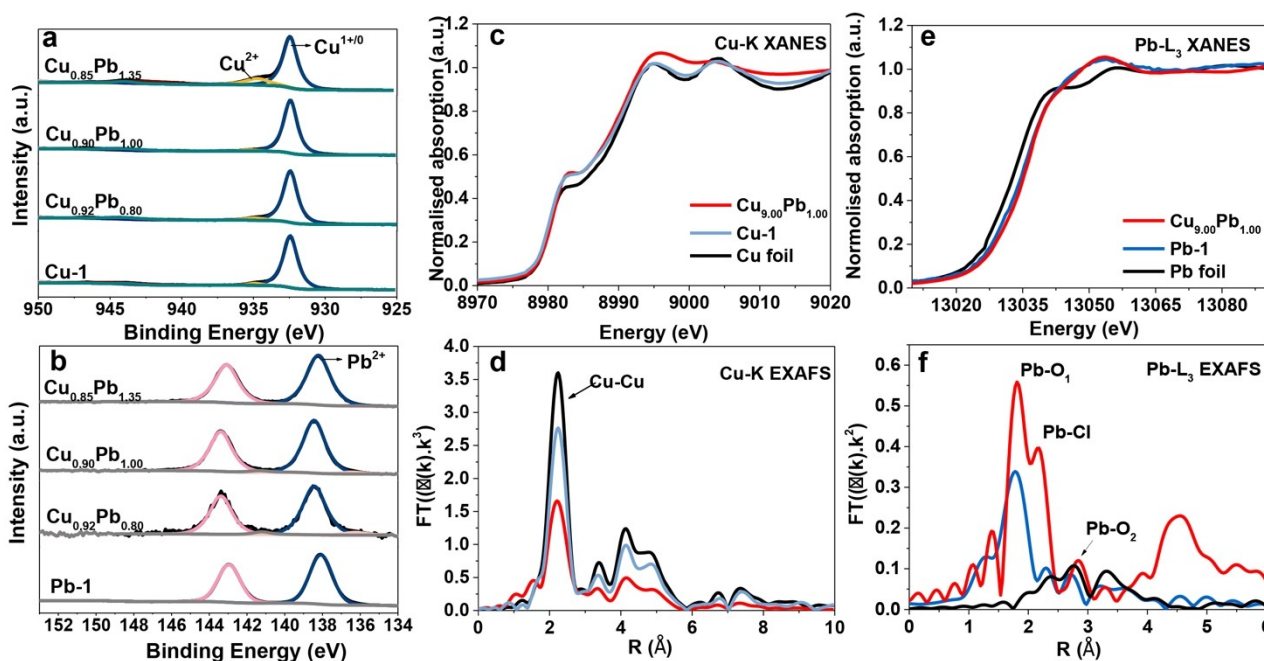


**Figure 2.** (a) Cu 2p and (b) Pb 4f X-ray Photoelectron Spectroscopy (XPS) data of different Cu<sub>x</sub>Pb<sub>y</sub> samples and Cu reference (Cu-1) and Pb reference (Pb-1). (c) Cu K edge X-ray Absorption Near Edge Spectroscopy (XANES) spectra of Cu<sub>9,00</sub>Pb<sub>1,00</sub>, Cu-1 and Cu foil and (d) the corresponding Extended X-Ray Absorption Fine Structure (EXAFS) spectra. (e) Pb L<sub>3</sub> edge XANES spectra of Cu<sub>9,00</sub>Pb<sub>1,00</sub>, Pb-1 and Pb foil, and (f) the corresponding EXAFS spectra. No Cu–Pb bonds were observed, indicating that the waste-derived bimetallic Cu<sub>x</sub>Pb<sub>y</sub> electrocatalysts are not alloys.

Cu and the absence of significant Cu–Pb bonds. This observation suggests that Cu and Pb do not form alloys under the present preparation conditions.<sup>[46]</sup> The coordination number (CN) of Cu–Cu bonds in Cu<sub>9,00</sub>Pb<sub>1,00</sub> is fitted to be 5.2 (Table S5), which is smaller than that of Cu foil (12.0) and Cu-1 (8.4), which is probably caused by the presence of abundant atomic defects within the Cu<sub>9,00</sub>Pb<sub>1,00</sub> structure.<sup>[47]</sup> In the Pb-L<sub>3</sub> XANES spectra (Figure 2e), it is suggested that Cu<sub>9,00</sub>Pb<sub>1,00</sub> contain a higher oxidation state than Pb<sup>2+</sup> in Pb-1 and Pb<sup>0</sup> in Pb foil, evidenced by a shift of the edge position to higher energy. Pb–O and Pb–Cl bonds are confirmed by the quantitative fitting results of the Pb-L<sub>3</sub> edge (Figure 2f and Figure S21b). The formation of Pb–Cl bonds could be from the NH<sub>4</sub>Cl involved in the electrocatalyst synthesis. Similarly, there is no Pb–Cu bond observed in Cu<sub>9,00</sub>Pb<sub>1,00</sub> (expected at larger bond lengths compared to the Cu–Cu bond), confirming that the pristine Cu<sub>9,00</sub>Pb<sub>1,00</sub> electrocatalyst is not an alloy, but instead consists of phase-separated Cu- and Pb-rich domains. Based on the observation above, we can draw the intermediate conclusion that Cu predominantly formed in the metallic state in the waste-derived electrocatalyst, while Pb is mainly present in its oxidized form and partially bonded with Cl<sup>−</sup> from the aqueous NH<sub>4</sub>Cl solution used for the chemical extraction procedure.

The eCO<sub>2</sub>R performance of the different Cu<sub>x</sub>Pb<sub>y</sub> electrocatalysts was explored using a three electrode H-type cell containing CO<sub>2</sub>-saturated 0.1 M KHCO<sub>3</sub> aqueous electrolyte solution. To analyze the product distribution and selectivity, electrolysis experiments were operated at constant potentials ranging from −0.85 to −1.25 V vs. RHE, and the products were analyzed with online GC and offline NMR measurements (representative results shown in Figure S22 and S23). Figure S24 and S25 show the *i*R-corrected potential dependent Faradaic efficiency (FE) profiles of CO, HCOOH, C<sub>2</sub>H<sub>4</sub> and H<sub>2</sub> for the different waste-derived Cu<sub>x</sub>Pb<sub>y</sub> electrodes. It was found that the Cu<sub>9,00</sub>Pb<sub>1,00</sub> electrode shows relatively lower H<sub>2</sub> and higher CO FE than all the other samples in the given potential window. The maximum FE of CO is 41.1% at −1.05 V vs. RHE, which is around four times higher than that of Cu-1 at this applied potential, suggesting synergistic effects between the Cu-rich and Pb-rich domains. Both Cu<sub>9,00</sub>Pb<sub>1,00</sub> and Cu-1 behave similarly in their stability test (Figure S26 and S27), and the observed degradation in catalytic performance over time could be attributed to partial detachment of active material during catalysis (Figure S28 and S29). The enhanced HCOOH formation is also observed in these Cu<sub>x</sub>Pb<sub>y</sub> catalysts, which can be attributed to the Pb species which are originally active for electrochemical CO<sub>2</sub> to HCOOH conversion. A very small amount of C<sub>2</sub>H<sub>4</sub> was also found in all Cu<sub>x</sub>Pb<sub>y</sub> samples due to the exposed active sites for ethylene production on the Cu surface.

To investigate the composition effect of the Cu<sub>x</sub>Pb<sub>y</sub> electrocatalysts in more detail, we compared the FE and production rate for the electrodes with different Cu/Pb metal ratios at a fixed potential of −1.05 V vs. RHE (Figure 3a, b). Compared to the pure Cu electrode (Cu-1), incorporation of a small amount of Pb (Cu<sub>9,20</sub>Pb<sub>0,80</sub>) enhances the eCO<sub>2</sub>R selectivity toward HCOOH and CO by twofold (31.8% and 22.8% for Cu<sub>9,20</sub>Pb<sub>0,80</sub>, respectively, compared to 17.1% and 9.7% for Cu-1) along with

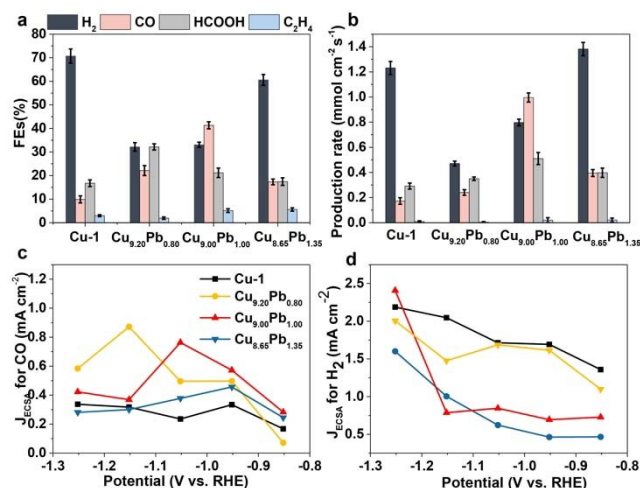


**Figure 3.** (a) Faradaic Efficiencies (FE) and (b) production rates of the main products (CO, HCOOH, H<sub>2</sub> and C<sub>2</sub>H<sub>4</sub>) for the different Cu<sub>x</sub>Pb<sub>y</sub> samples at −1.05 V vs. RHE. ECSA-normalized partial current density of (c) CO and (d) H<sub>2</sub> for the different Cu<sub>x</sub>Pb<sub>y</sub> catalysts at varying cathodic potentials.

a lower H<sub>2</sub> production (around 30.1% for Cu<sub>9,20</sub>Pb<sub>0,80</sub> compared to 70.9% for Cu-1). The CO production is further enhanced when a slightly higher amount of Pb is introduced (Cu<sub>9,00</sub>Pb<sub>1,00</sub>), reaching over 41.1% FE for CO. In Cu<sub>8,65</sub>Pb<sub>1,35</sub>, both CO and HCOOH productions are hindered, and a dramatic increase of H<sub>2</sub> FE is observed (60.6%, comparable to 70.8% for Cu-1). This leads to a volcano-shaped dependence of the CO selectivity based on the amount of Pb present in the Cu<sub>x</sub>Pb<sub>y</sub> electrodes (Figure 3a). A similar trend is also found in the production rate distribution (Figure 3b), confirming the compositional effect on CO selectivity. In general, the partial current density normalized by the geometric surface area of the electrodes does not reflect the intrinsic activity.<sup>[48]</sup> To understand the intrinsic activity of these waste-derived Cu<sub>x</sub>Pb<sub>y</sub> electrocatalysts, we analyzed the Electrochemical Surface Area (ECSA) (Figure S30 and S31, Table S6) and evaluated their ECSA-normalized partial current densities for CO (Figure 3c) and H<sub>2</sub> (Figure 3d). We note that the ECSA measurements were not conducted under catalytic conditions, and that surface transformation under more negative potentials may lead to changes in ECSA, but are difficult to assess under catalytic conditions. In agreement with the trend that we found in the FE and production rate (Figure 3a, b), Cu<sub>9,00</sub>Pb<sub>1,00</sub> shows a significantly higher ECSA-normalized activity for CO (Figure 3c) compared to Cu-1, Cu<sub>8,65</sub>Pb<sub>1,35</sub> and Cu<sub>9,20</sub>Pb<sub>0,80</sub>, along with the lowest activity for H<sub>2</sub> at −1.05 V vs. RHE (Figure 3d). This trend indicates that an optimal amount of Pb co-existing with Cu provides a means to suppress the competitive HER in favor of CO production.

To analyze the observed effect of the Cu/Pb ratio on the catalytic performance in more detail, we monitored the structural changes in these Cu<sub>x</sub>Pb<sub>y</sub> catalysts at the eCO<sub>2</sub>R onset by *in situ* Raman spectroscopy measurements. These *in situ* Raman measurements were performed in CO<sub>2</sub>-saturated 0.1 M KHCO<sub>3</sub> electrolyte solution. The CV curves were achieved by scanning between −1.0 V to 1.6 V vs. RHE using a scan rate of

50 mV/s, and Raman spectra were collected at a rate of one spectrum per second in order to construct the Raman spectroscopy heatmaps as a function of applied potential (Figure 4). As shown in Figure 4a, the first reduction peak occurs at 0.2 V vs. RHE for the  $\text{Cu}_{9.20}\text{Pb}_{0.80}$  electrode, which is attributed to the reduction of  $\text{Cu}^+$  to  $\text{Cu}^0$ .<sup>[49–51]</sup> The corresponding Raman spectroscopy heatmap (Figure 4b) reveals that the signals associated with  $\text{CuO}_x$  (at 504 and 619  $\text{cm}^{-1}$ ) disappear at 0.13 V vs. RHE, corresponding to the end of the  $\text{Cu}^+$  to  $\text{Cu}^0$  reduction peak in the CV (indicated with a dashed line in Figure 4a). When an increased cathodic bias is applied, a second reduction peak appears at  $-0.03$  V vs. RHE. Since  $\text{Cu}^+$  is already fully reduced to  $\text{Cu}^0$ , as evidenced by the *in situ* Raman spectroscopy measurement, this reduction peak is tentatively ascribed to the *in situ* reduction of  $\text{Pb}^{2+}$  species. A similar phenomenon of  $\text{Cu}^+$  reduction to  $\text{Cu}^0$  can be found in the *in situ* Raman spectroscopy heatmaps for  $\text{Cu}_{9.00}\text{Pb}_{1.00}$  and  $\text{Cu}_{8.65}\text{Pb}_{1.35}$ , although the absolute reduction potential varies slightly. However, there are two Pb reduction peaks observed in the CV of the  $\text{Cu}_{9.00}\text{Pb}_{1.00}$  electrode after the disappearance of the  $\text{CuO}_x$  Raman signal (Figure 4c, d). These two reduction features in the CV potentially correspond to two different types of Pb, which is well in line with the Pb-L<sub>3</sub> edge EXAFS results (Figure 2f) that indicated the presence of Pb–O and Pb–Cl bonds. In  $\text{Cu}_{8.65}\text{Pb}_{1.35}$  (Figure 4c, f), the Cu reduction peak shifts to more negative cathodic bias

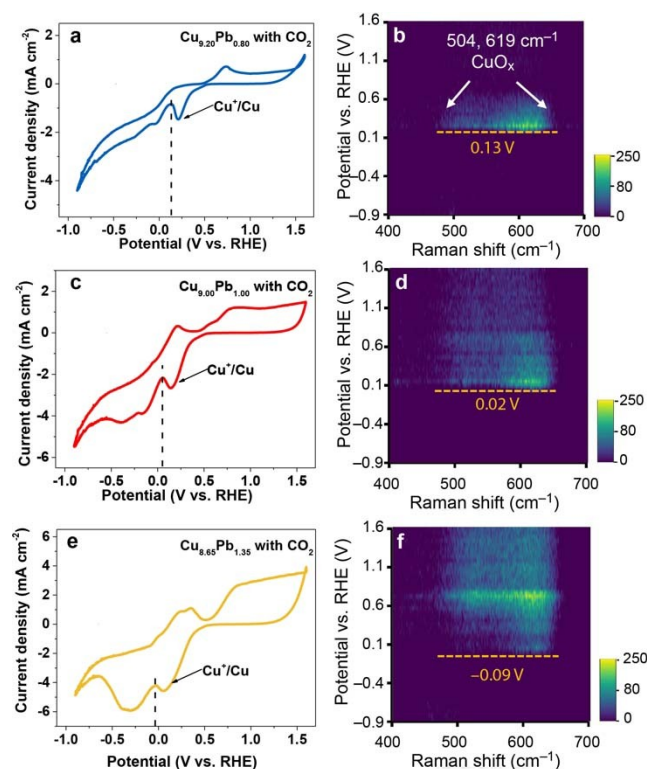
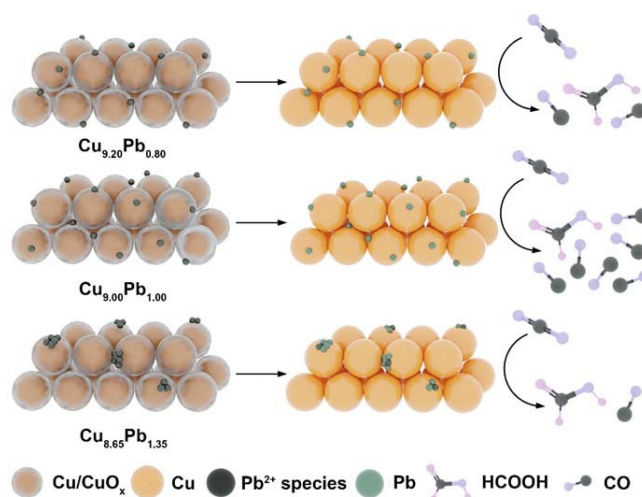


**Figure 4.** Cyclic Voltammetry (CV) curves and *in situ* Raman spectra of (a, b)  $\text{Cu}_{9.20}\text{Pb}_{0.80}$ , (c, d)  $\text{Cu}_{9.00}\text{Pb}_{1.00}$  and (e, f)  $\text{Cu}_{8.65}\text{Pb}_{1.35}$  waste-derived electrocatalysts, showing a shift of the Cu reduction onset to more negative cathodic bias when more Pb is present in the electrocatalyst. Dashed lines (black and yellow) represent the potentials at which the Cu reduction is finished, as evidenced by the *in situ* Raman spectra.

compared to  $\text{Cu}_{9.20}\text{Pb}_{0.80}$  and  $\text{Cu}_{9.00}\text{Pb}_{1.00}$ . Only one reduction peak of Pb is found in this CV curve, implying that the reduction of Pb species is inhibited under the electrochemical reduction conditions. The observed shift of the Cu reduction peak to more negative cathodic bias suggests that more driving force is needed for the reduction of  $\text{Cu}^+$  to the metallic state when too much Pb coexists with Cu. The difficulty of Pb reduction in  $\text{Cu}_{8.65}\text{Pb}_{1.35}$  can be ascribed to the aggregation of Pb species (Figure S14), while the aggregation is absent in the other two samples (Figure S13 and Figure 1e).<sup>[52]</sup> To confirm the *in situ* electrochemical reduction of Pb and Cu species, we analyzed Cu LMM spectroscopy and observed that the contribution of  $\text{Cu}^0$  increases after catalysis compared to before catalysis (Figure S32). This is further corroborated by the XRD pattern of the  $\text{Cu}_{9.00}\text{Pb}_{1.00}$  electrocatalyst before and after catalysis (Figure S33), where we observe that the reflections of  $\text{Cu}_2\text{O}$  have disappeared after  $\text{eCO}_2\text{R}$  and only metallic Cu reflections are present after one hour of electrolysis.

The relationship between metal ratio and performance of the waste-derived  $\text{Cu}_x\text{Pb}_y$  electrocatalysts is summarized in Scheme 2. First, when a small amount of Pb is present in the bimetallic catalyst ( $\text{Cu}_{9.20}\text{Pb}_{0.80}$ ), hydrogen evolution is suppressed and the formation of HCOOH and CO is enhanced. As shown in Figure S21,  $\text{H}_2$  evolution is dominant in pure Cu (Cu-1) electrodes, while pure Pb (Pb-1) mainly produces HCOOH. Therefore, the enhancement of the CO formation for the bimetallic electrodes cannot be solely ascribed to Cu or Pb domains in the bimetallic electrocatalyst. Instead, the combination of *in situ* reduced metallic Cu and Pb, evidenced by CV and *in situ* Raman spectroscopy results, is necessary for enhanced CO formation. The enhancement of the CO formation reaches a maximum of 41.1% at  $-1.05$  V vs. RHE when more Pb is present in the form of a Cu/Pb ratio of 9.0, resulting from the formation



**Scheme 2.** Schematic representation of the pristine waste-derived  $\text{Cu}_x\text{Pb}_y$  electrocatalysts and their compositional transformation under  $\text{eCO}_2\text{R}$  conditions.  $\text{Cu}_{9.20}\text{Pb}_{0.80}$  and  $\text{Cu}_{9.00}\text{Pb}_{1.00}$  have the ability to form metallic Pb under reaction conditions, thereby enhancing the selectivity for C<sub>1</sub> products through a nanoscale synergistic effect between Cu and Pb. This synergistic effect is relatively weaker in  $\text{Cu}_{8.65}\text{Pb}_{1.35}$  since the formation of metallic Pb is prohibited, which results in a similar catalytic performance as pure Cu.

of more metallic Pb and the subsequent stronger Cu–Pb synergy under reaction conditions. The increase in HCOOH FE for  $\text{Cu}_{9,00}\text{Pb}_{1,00}$  compared to  $\text{Cu}_{9,20}\text{Pb}_{0,80}$  suggests that the HCOOH formation is intrinsically promoted by Pb species.<sup>[53–56]</sup> However, when even more Pb is introduced, the enhancement effect for CO production is weakened, which is explained by the lower tendency of  $\text{Cu}_{8,65}\text{Pb}_{1,35}$  to form metallic Cu and Pb under these reaction conditions. Therefore, CO production dramatically decreases in  $\text{Cu}_{8,65}\text{Pb}_{1,35}$  due to the absence of a synergistic effect between metallic Cu and Pb, and the catalytic performance is similar to pure Cu (Figure 3a).<sup>[57–60]</sup> The small decrease in HCOOH formation for  $\text{Cu}_{8,65}\text{Pb}_{1,35}$  is caused by the aggregation of  $\text{Pb}^{2+}$  species which is also responsible for their inferior reducibility (Figure S14). Overall, we have found that coexistence of Cu and Pb in Cu-based waste-derived bimetallic electrocatalysts promotes the formation of CO through a synergistic effect between *in situ* reduced Pb and Cu, while the presence of a larger amount of PbO in the pristine electrocatalyst hampers the *in situ* formation of metallic Cu and Pb, which limits the synergistic effect and lowers the electrocatalytic performance.

## Conclusions

We have prepared a series of copper-lead ( $\text{Cu}_x\text{Pb}_y$ ,  $x+y=10$ ) materials from industrial metallurgical waste, which were evaluated for the electrochemical  $\text{CO}_2$  reduction reaction. The Cu and Pb species were obtained from the industrial waste through chemical extraction with ammonium chloride, and the composition of the waste-derived electrocatalysts was tailored through the electrodeposition conditions. The composition of the pristine waste-derived electrocatalysts was analyzed with XRD, XPS and XAS, which revealed that the bimetallic electrocatalysts consist of  $\text{Cu}^0$ ,  $\text{Cu}^+$  and  $\text{Pb}^{2+}$  domains, and no alloy formation was observed. Improved selectivity towards CO was observed in these bimetallic systems compared to pure Cu. The optimized  $\text{Cu}_{9,00}\text{Pb}_{1,00}$  electrocatalyst showed a fourfold improvement of CO formation compared to pure Cu under the same electrochemical conditions. Through *in situ* Raman spectroscopy, it was revealed that the reducibility of pristine  $\text{Cu}^{1+}$  and  $\text{Pb}^{2+}$  species into metallic  $\text{Cu}^0$  and  $\text{Pb}^0$  played a crucial role in the enhanced formation of CO. With a proper amount of Pb coexisting with Cu, a synergy between *in situ* reduced Cu and Pb facilitated enhanced CO selectivity, whereas these reduction processes were hampered when the amount of Pb species was increased because of Pb species aggregation, resulting in a decrease of CO selectivity and an increase in hydrogen evolution reaction. Our results show the potential of industrial waste-derived bimetallic electrocatalysts for the rational and sustainable design of  $\text{C}_1$  product selective  $\text{eCO}_2\text{R}$  electrocatalysts.

## Experimental Section

### Industrial waste extraction

The studied fayalite slags were provided by Aurubis Beerse NV. Four different extraction strategies were applied to the fayalite slags under study. Before taking these treatments, the fayalite slags (0.5–1.0 cm diameter) were ground into fine powders with a particle size of 75  $\mu\text{m}$ . Acid treatment was conducted by mixing sulfuric acid and the ground fayalite slags. When a concentrated sulfuric acid was used, the fayalite slags almost stayed unchanged because of the passivation. We also tried 5 M sulfuric acid with and without heating. A black gel was formed and difficult to be further separated when heating at 40 °C for 1 h, whereas no obvious change was observed under 25 °C. To remove silicon from the residue system, alkali (NaOH solution) was applied to the fayalite slags. A certain amount of the ground powders was added to the NaOH aqueous solution (from 1 M to 10 M), stirring for a certain time (from 2 h to 24 h). The treatment temperatures ranged from 50 °C to 150 °C. Filtration was applied to separate liquid and solid phases. After the treatment, iron oxides were formed on the surface of fayalite slag with an increased roughness (Figures S3 and S4). However, the main phase of the treated samples remains fayalite structure (Figure S5) and inactive for most possible applications. Thermal treatment was employed by annealing the ground fayalite slags at temperatures ranging from 500 °C to 1100 °C for 2 h in air. Although the structure of the fayalite slags has transferred into iron oxides and  $\text{SiO}_2$  (Figure S6) under the temperature as high as 1100 °C, the whole chemical environment inside the treated samples was complicated because all impurities still remain. We tried to dissolve the thermal-treated slags with acid treatment further. Unfortunately, the degree of passivation is higher than the untreated one. The only working treatment is the complexing treatment. Different amounts (1, 2, 3, 4, 5 g) of ground powders were mixed with 12 mL  $\text{NH}_4\text{Cl}$  aqueous solution with different concentration (1, 3, 5 M), followed by stirring for 24 h at room temperature. After filtration, a blue solution was collected. 0.5 mL of the filtrate was used for UV-Vis spectroscopy measurements, to analyze the complex concentration of  $[\text{Cu}(\text{NH}_3)_4]^{2+}/[\text{CuCl}_4]^{2-}$ . As suggested in Figure S7, the strongest intensity can be obtained in the filtrate collected from the combination of 4g fayalite slags and 3 M  $\text{NH}_4\text{Cl}$  aqueous solution, suggesting the highest extraction efficiency.

### Catalyst preparation

The Cu-based electrocatalysts were obtained by one-step electrodeposition. 12 mL filtrate, collected from the complexing extraction using 4g fayalite slags and 3 M  $\text{NH}_4\text{Cl}$  solution, was diluted by mixing with 12 mL deionized water. The diluted filtrate (24 mL) was used as electrolyte for all samples, except for control samples Cu-1 and Pb-1. The  $\text{NH}_4\text{Cl}$  can be reused for subsequent extraction of metals from industrial waste residues. Carbon paper (effective geometric surface area 1  $\text{cm}^2$ ) was used as substrate during electrodeposition, Pt wire was used as counter electrode and Ag/AgCl was used as reference electrode (ET069-3,  $-0.205$  V vs. SHE, eDAQ). The electrocatalysts were prepared by applying various potentials ( $-0.6$  V,  $-0.8$  V and  $-1.0$  V vs. Ag/AgCl) for 600 s with a stirring rate of 350 rpm to achieve  $\text{Cu}_{9,20}\text{Pb}_{0,80}$ ,  $\text{Cu}_{9,00}\text{Pb}_{1,00}$  and  $\text{Cu}_{8,65}\text{Pb}_{1,35}$ , respectively. The obtained samples were washed with MilliQ water before the electrochemical measurements. The reference sample Cu-1 was obtained by electrodeposition at  $-0.8$  V vs. Ag/AgCl from an aqueous solution containing 0.1 M  $\text{CuCl}_2$  and 3 M  $\text{NH}_4\text{Cl}$ . The reference sample Pb-1 was prepared through galvanostatic electrodeposition at  $-10$  mA in 0.1 M  $\text{PbCl}_2$  solution.

## Characterization

UV-Vis spectroscopy was performed by using an Avantes DH-2000-BAL Deuterium lamp and an Avantes StarLine AvaSpec-2048 L spectrometer using a liquid-immersed probe head. The spectra were obtained in the range 200–1100 nm. The elemental composition of the pristine samples was characterized by Inductively Coupled Plasma-Optical Emission Spectrometry (ICP-OES, PerkinElmer Optima 8300 Optical Emission Spectrometer). An average of three samples was used. The fayalite slags were dissolved in aqua regia for 48 hours, followed by a filtration to remove the undissolved species. Electrodeposited samples were dissolved in 65% HNO<sub>3</sub> (2 mL) before oxidation. The obtained solutions were diluted with 5% HNO<sub>3</sub> to achieve optimal measurement ranges. Atomic Force Microscopy (AFM) measurements were performed with a Bruker Multimode microscope instrument, using silicon NSC-16 SCANASYST-AIR ( $F=0.4\text{ N m}^{-1}$ ,  $f_{\text{res}}=70\text{ kHz}$ ) in ScanAsyst mode. X-Ray Diffraction (XRD) measurements were performed on a Bruker D8 Phaser diffractometer, equipped with a Cu K $\alpha$  source ( $\lambda=1.54056\text{ \AA}$ ). The morphology and elemental distribution were determined with Scanning Electron Microscopy (SEM, FEI Helios NanoLab 600) and high-resolution High Angle Annular Dark Field Scanning Transmission Electron Microscopy (HAADF-STEM) and coupled STEM Energy Dispersive X-ray (STEM-EDX) measurement (FEI Titan<sup>3</sup>, 200 keV). To do this, the catalyst materials were stripped off the carbon paper electrodes by sonication in absolute ethanol for the HAADF-STEM measurements. In X-ray Photoelectron Spectroscopy (XPS) measurement, a K-Alpha X-ray photoelectron spectrometer by ThermoFisher scientific with an aluminum ( $K=1486.68\text{ eV}$ ) X-ray source was used to collect the X-ray photoelectron spectra. All spectra were calibrated with reference to the C 1s at 284.8 eV. The curve fitting was carried out using Shirley/Linear background and a combination of Gaussian and Lorentzian functions. X-ray Absorption Spectroscopy (XAS) measurements were performed by the Beijing Synchrotron Radiation Facility (1W1B, BSRF) at the Cu K-edge and Pb L<sub>3</sub>-edge.

## In situ Raman spectroscopy

The *in situ* Raman spectra were collected using a Renishaw InVia Raman microscope and 785 nm excitation laser, coupled with a Nikon N40X-NIR water-dipping objective. To avoid laser damage, the laser power was set to below 1.5 mW. The time interval for each spectrum is 1 s for all measured samples. An Autolab PGSTAT 101 potentiostat was used for cyclic voltammetry (CV) measurement which was carried out under a scanning rate of 50 mV s<sup>-1</sup> in CO<sub>2</sub> saturated 0.1 M KHCO<sub>3</sub> electrolyte solution (pH 6.8), from -1.0 V to 1.6 V vs. RHE.

## Electrochemical measurements

The Ivium compactstat.h10800 potentiostat was used for all electrochemical measurements. The samples were loaded in a standard three-electrode system in a two-compartment H-cell separated by a proton exchange membrane (Nafion 117, Dupont). Fresh samples were used for the activity measurements at different applied potentials, and averaged over four measurements. Ag/AgCl (ET072-3, -0.205 V vs. SHE) and a Pt-mesh were employed as reference electrode and counter electrode, respectively. 0.1 M KHCO<sub>3</sub> aqueous solution saturated with CO<sub>2</sub> (pH=6.8) was applied as electrolyte for all CO<sub>2</sub> reduction experiments. During the experiments, CO<sub>2</sub> was continuously delivered into the cathodic compartment at a constant rate of 8.7 mL min<sup>-1</sup>. The as-prepared samples were employed as working electrode directly, and held for 40 min at least under different constant biases (-0.85 V, -0.95 V, -1.05 V, -1.15 V, -1.25 V vs. RHE). To calculate the Electrochemical Surface

Area (ECSA), the double-layer capacitance ( $C_{\text{dl}}$ ) was determined through the Cyclic Voltammetry (CV) measurements in the non-Faradaic region at 30, 50, 70, 100, 150 mV s<sup>-1</sup> scan rate by a linear fit of the charging current. The ECSA of as-prepared sample was obtained by subtracting  $C_{\text{dl}}$  of carbon paper and normalizing the  $C_{\text{dl}}$  difference to that of Cu foil. Regarding the  $iR$  correction, the solution resistance was calculated by Electrochemical Impedance Spectroscopy (EIS) with a frequency range of 0.01 to 100 kHz.

The measured potential values were converted to the Reversible Hydrogen Electrode (RHE) using Equation (1).

$$E(\text{vs. RHE}) = E(\text{vs. Ag/AgCl}) + 0.205\text{ V} + 0.059 \times \text{pH} \quad (1)$$

## Products analysis

The gas products at each fixed potential were quantified by an online Gas Chromatograph (GC) equipped with a Thermal Conductivity Detector (TCD) and a Flame Ionization Detector (FID). <sup>1</sup>H Nuclear Magnetic Resonance (NMR) spectroscopy was employed to determine the liquid products using water suppression mode. 0.5 mL of electrolyte was mixed with 0.1 mL of deuterated water (D<sub>2</sub>O) as lock solvent. Then, 0.05  $\mu\text{L}$  of dimethyl sulfoxide (DMSO) was used as the internal reference.

The Faradaic Efficiency (FE) of gas products was calculated using the following equation.

$$FE = \frac{n \cdot F \cdot c \cdot f}{Vm \cdot I \cdot \frac{60\text{sec}}{\text{min}} \cdot 1000000\text{ppm}} \times 100\%$$

Where  $n$  represents the number of electrons involved to produce the related products from CO<sub>2</sub> or H<sub>2</sub>O (e.g., 2 for CO and H<sub>2</sub>, 12 for C<sub>2</sub>H<sub>4</sub>);  $F$  is the Faraday constant (96485 C mol<sup>-1</sup>);  $c$  is the concentration of the product measured by GC;  $f$  is the gas flow rate (mL min<sup>-1</sup>);  $I$  is the average measured current in 1 min (A);  $Vm$  is the volume of 1 mol gas at reaction temperature and pressure (24451 mL mol<sup>-1</sup>)

The FE of liquid products was calculated by using Equation (2).

$$FE = \frac{n \cdot F \cdot M \cdot V}{I \cdot t} \quad (2)$$

Where  $n$  is the number of electrons transferred to form the desired product (e.g., 2 for HCOOH);  $F$  is the Faraday constant (96485 C mol<sup>-1</sup>);  $M$  is the Molar concentration of the liquid product (mol L<sup>-1</sup>);  $V$  is the liquid volume (L);  $I$  is the average measured current in 1 minute (A);  $t$  is the duration time (s).

Production rate of all products were calculated by using Equation (3):

$$\text{production rate} = \frac{FE \cdot I}{n \cdot F \cdot S} \quad (3)$$

Where  $n$  represents the number of electrons needed to produce the related products;  $F$  is the Faraday constant (96485 C mol<sup>-1</sup>);  $I$  is the average measured current in 1 min (A);  $S$  represents the geometric area of the electrode (cm<sup>2</sup>).



## Acknowledgements

S.Y and B.M.W. acknowledge support from the EU Framework Programme for Research and Innovation Horizon 2020 (SOCRA-TES-721385; project website: <http://etn-socrates.eu/>). W.v.d.S., M.C.F. and B.M.W. acknowledge support from the Strategic UU-TU/e Alliance project 'Joint Centre for Chemergy Research'. S.B. acknowledges support from the European Research Council (ERC Consolidator Grant #815128 REALNANO). S.A. and T.A. acknowledge funding from the University of Antwerp Research fund (BOF). The Beijing Synchrotron Radiation Facility (1W1B, BSRF) is acknowledged for the beamtime. We are grateful to Annelies van der Bok and Bas Salzmann (Condensed Matter and Interfaces, Utrecht University, UU) for the support with the ICP-OES measurements. The authors thank dr. Robin Geitenbeek, Nikos Nikolopoulos, Ioannis Nikolopoulos, Jochem Wijten and Joris Janssens (Inorganic Chemistry and Catalysis, UU) for helpful discussions and technical support. The authors also thank Yuang Piao (Materials Chemistry and Catalysis, UU) for the help in the preparation of the figures of the article.

## Conflict of Interest

The authors declare no conflict of interest.

## Data Availability Statement

The data that support the findings of this study are available from the corresponding author upon reasonable request.

- [1] B. M. Tackett, E. Gomez, J. G. Chen, *Nat. Catal.* **2019**, *2*, 381–386.
- [2] J. Artz, T. E. Müller, K. Thenert, J. Kleinekorte, R. Meys, A. Sternberg, A. Bardow, W. Leitner, *Chem. Rev.* **2018**, *118*, 434–504.
- [3] D. Gao, R. M. Arán-Ais, H. S. Jeon, B. Roldan Cuenya, *Nat. Catal.* **2019**, *2*, 198–210.
- [4] D. Raciti, C. Wang, *ACS Energy Lett.* **2018**, *3*, 1545–1556.
- [5] P. Sebastián-Pascual, S. Mezzavilla, I. E. L. Stephens, M. Escudero-Escribano, *ChemCatChem* **2019**, *11*, 3626–3645.
- [6] M. Ma, K. Djanashvili, W. A. Smith, *Angew. Chem. Int. Ed.* **2016**, *55*, 6680–6684; *Angew. Chem.* **2016**, *128*, 6792–6796.
- [7] R. Kortlever, J. Shen, K. J. P. Schouten, F. Calle-Vallejo, M. T. M. Koper, *J. Phys. Chem. Lett.* **2015**, *6*, 4073–4082.
- [8] J. He, K. E. Dettelbach, A. Huang, C. P. Berlinguette, *Angew. Chem. Int. Ed.* **2017**, *4*, 16806–16809.
- [9] A. Vasileff, C. Xu, Y. Jiao, Y. Zheng, S. Qiao, *Chem* **2018**, *4*, 1809–1831.
- [10] H. Guo, Y. Hou, A. Dutta, S. R. Waldvogel, P. Broekmann, *ChemElectroChem* **2019**, *6*, 2324–2333.
- [11] S. Stojković, G. A. El-Nagar, F. Firsche, L. C. Pardo, L. Choubrac, M. Najdoski, M. T. Mayer, *ACS Appl. Mater. Interfaces* **2021**, *13*, 38161–38169.
- [12] B. Zhang, K. Hung Lai, B. Wang, Z. Wang, *Resour. Conserv. Recycl.* **2018**, *139*, 40–47.
- [13] M. Palmiotto, E. Fattore, V. Paiano, G. Celeste, A. Colombo, E. Davoli, *Environ. Int.* **2014**, *68*, 16–24.
- [14] A. Yilmaz, E. Atmaca, *Environ. Geol.* **2006**, *50*, 677–689.
- [15] S. Mor, K. Ravindra, R. P. Dahiya, A. Chandra, *Environ. Monit. Assess.* **2006**, *118*, 435–456.
- [16] J. Albo, A. Sáez, J. Solla-Gullón, V. Montiel, A. Irabien, *Appl. Catal. B: Environmental* **2015**, *177*, 709–717.
- [17] J. Huang, M. Mensi, E. Oveisi, V. Mantella, R. Buonsanti, *J. Am. Chem. Soc.* **2019**, *141*, 2490–2499.
- [18] J. Albo, D. Vallejo, G. Beobide, O. Castillo, P. Castaço, *ChemSusChem* **2017**, *10*, 1100–1109.
- [19] C. J. Chang, S. C. Lin, H. C. Chen, J. Wang, K. J. Zheng, Y. Zhu, H. M. Chen, *J. Am. Chem. Soc.* **2020**, *142*, 12119–12132.
- [20] C. G. Morales-Guio, E. R. Cave, S. A. Nitopi, J. T. Feaster, L. Wang, K. P. Kuhl, A. Jackson, N. C. Johnson, D. N. Abram, T. Hatsukade, C. Hahn, T. F. Jaramillo, *Nat. Catal.* **2018**, *1*, 764–771.
- [21] S. Nitopi, E. Bertheussen, S. B. Scott, X. Liu, A. K. Engstfeld, S. Horch, B. Seger, I. E. L. Stephens, K. Chan, C. Hahn, J. K. Nørskov, T. F. Jaramillo, I. Chorkendorff, *Chem. Rev.* **2019**, *119*, 7610–7672.
- [22] J. E. Pander, M. F. Baruch, A. B. Bocarsly, *ACS Catal.* **2016**, *6*, 7824–7833.
- [23] C. Kim, T. Möller, J. Schmidt, A. Thomas, P. Strasser, *ACS Catal.* **2019**, *9*, 1482–1488.
- [24] Y. Kwon, J. Lee, *Electrocatalysis* **2010**, *1*, 108–115.
- [25] A. Bagger, W. Ju, A. S. Varela, P. Strasser, J. Rossmeisl, *ChemPhysChem* **2017**, *18*, 3266–3273.
- [26] M. Schreier, F. Héroguel, L. Steier, S. Ahmad, J. S. Luterbacher, M. T. Mayer, J. Luo, M. Grätzel, *Nat. Energy* **2017**, *2*, 17087.
- [27] W. Lv, J. Zhou, J. Bei, R. Zhang, L. Wang, Q. Xu, W. Wang, *Appl. Surf. Sci.* **2017**, *393*, 191–196.
- [28] S. Rasul, D. H. Anjum, A. Jedidi, Y. Minenkov, L. Cavallo, K. Takanabe, *Angew. Chem. Int. Ed.* **2015**, *127*, 2174–2178.
- [29] M. Bernal, A. Bagger, F. Scholten, I. Sinev, A. Bergmann, M. Ahmadi, J. Rossmeisl, B. R. Cuenya, *Nano Energy* **2018**, *53*, 27–36.
- [30] Z. Chang, S. Huo, W. Zhang, J. Fang, H. Wang, *J. Phys. Chem. C* **2017**, *121*, 11368–11379.
- [31] Z. B. Hoffman, T. S. Gray, K. B. Moraveck, T. B. Gunnoe, G. Zangari, *ACS Catal.* **2017**, *7*, 5381–5390.
- [32] J. P. Grote, A. R. Zeradjanin, S. Cherevko, A. Savan, B. Breitbach, A. Ludwig, K. J. J. Mayrhofer, *J. Catal.* **2016**, *343*, 248–256.
- [33] S. Lee, G. Park, J. Lee, *ACS Catal.* **2017**, *7*, 8594–8604.
- [34] D. Kim, J. Resasco, Y. Yu, A. M. Asiri, P. Yang, *Nat. Commun.* **2014**, *5*, 4948.
- [35] B. Morosin, A. C. Larson, *Acta Crystallogr.* **1969**, *B25*, 1417–1419.
- [36] S. Yancoillie, K. Pierloot, *J. Phys. Chem. A* **2008**, *112*, 4011–4019.
- [37] J. Li, A. Xu, F. Li, Z. Wang, C. Zou, C. M. Gabardo, Y. Wang, A. Ozden, Y. Xu, D. H. Nam, Y. Lum, J. Wicks, B. Chen, Z. Wang, J. Chen, Y. Wen, T. Zhuang, M. Luo, X. Du, T. K. Sham, B. Zhang, E. H. Sargent, D. Sinton, *Nat. Commun.* **2020**, *11*, 3685.
- [38] A. A. Permyakova, J. Herranz, M. El Kazzi, J. S. Diercks, M. Povia, L. R. Mangani, M. Horisberger, A. Pătru, T. J. Schmidt, *ChemPhysChem* **2019**, *20*, 3120–3127.
- [39] W. W. Wang, W. Z. Yu, P. P. Du, H. Xu, Z. Jin, R. Si, C. Ma, S. Shi, C. J. Jia, C. H. Yan, *ACS Catal.* **2017**, *7*, 1313–1329.
- [40] L. Liu, Z. Yao, Y. Deng, F. Gao, B. Liu, L. Dong, *ChemCatChem* **2011**, *3*, 978–989.
- [41] Y. Wang, Y. Zhang, Y. Feng, X. Zhang, J. Liu, W. Hou, J. Jia, B. Zhang, *Iop. Conf. Ser. Mater. Sci. Eng.* **2019**, *490*, 022067.
- [42] I. S. Zhidkov, A. F. Akbulatov, A. I. Kukhareno, S. O. Cholakh, K. J. Stevenson, P. A. Troshinb, E. Z. Kurmaev, *Mendeleev Commun.* **2018**, *28*, 381–383.
- [43] C. J. Yang, L. X. Zhao, X. Zhang, D. C. Zhai, Y. Gu, *Prot. Met. Phys. Chem. Surfaces* **2020**, *56*, 302–310.
- [44] Z. Jin, C. Liu, K. Qi, X. Cui, *Sci. Rep.* **2017**, *7*, 39695.
- [45] X. P. Cui, K. J. Jiang, J. H. Huang, X. Q. Zhou, M. J. Su, S. G. Li, Q. Q. Zhang, L. M. Yang, Y. L. Song, *Chem. Commun.* **2015**, *51*, 1457–1460.
- [46] S. Yang, Q. He, C. Wang, H. Jiang, C. Wu, Y. Zhang, T. Zhou, Y. Zhou, L. Song, *J. Mater. Chem. A* **2018**, *6*, 11281–11287.
- [47] J. Wu, R. M. Yadav, M. Liu, P. P. Sharma, C. S. Tiwary, L. Ma, X. Zou, X. D. Zhou, B. I. Yakobson, J. Lou, P. M. Ajayan, *ACS Nano* **2015**, *9*, 5364–5371.
- [48] M. Łukaszewski, M. Soszko, A. Czerwiński, *Int. J. Electrochem. Sci.* **2016**, *11*, 4442–4469.
- [49] H. An, L. Wu, L. Mandemaker, S. Yang, J. de Ruiter, J. Wijten, J. Janssens, T. Hartman, W. van der Stam, B. M. Weckhuysen, *Angew. Chem. Int. Ed.* **2021**, *60*, 16576–16584.
- [50] L. D. Burke, M. J. G. Ahern, T. G. Ryan, *J. Electrochem. Soc.* **1990**, *137*, 553–561.
- [51] M. Ma, K. Djanashvili, W. A. Smith, *Phys. Chem. Chem. Phys.* **2015**, *17*, 20861–20867.
- [52] P. Panagiotopoulou, A. Christodoulakis, D. I. Kondarides, S. Boghosian, *J. Catal.* **2006**, *240*, 114–125.
- [53] C. H. Lee, M. W. Kanan, *ACS Catal.* **2015**, *5*, 465–469.
- [54] M. J. W. Blom, V. Smulders, W. P. M. van Swaaij, S. R. A. Kersten, G. Mul, *Appl. Catal. B: Environmental* **2020**, *268*, 118420.

- [55] B. Innocent, D. Liaigre, D. Pasquier, F. Ropital, J. M. Léger, K. B. Kokoh, *J. Appl. Electrochem.* **2009**, *39*, 227–232.
- [56] S. Ha, R. Larsen, R. I. Masel, *J. Power Sources* **2005**, *144*, 28–34.
- [57] S. Chu, S. Hong, J. Masa, X. Li, Z. Sun, *Chem. Commun.* **2019**, *55*, 12380–12383.
- [58] L. Lin, H. Li, C. Yan, H. Li, R. Si, M. Li, J. Xiao, G. Wang, X. Bao, *Adv. Mater.* **2019**, *31*, 1903470.
- [59] W. Xie, H. Li, G. Gui, J. Li, Y. Song, S. Li, X. Zhang, J. Y. Lee, M. Shao, M. Wei, *Angew. Chem. Int. Ed.* **2021**, *60*, 7382–7388.
- [60] Y. Li, B. Wei, M. Zhu, J. Chen, Q. Jiang, B. Yang, Y. Hou, L. Lei, Z. Li, R. Zhang, Y. Lu, *Adv. Mater.* **2021**, *33*, 2102212.

---

Manuscript received: June 13, 2022  
Revised manuscript received: June 27, 2022  
Accepted manuscript online: June 28, 2022  
Version of record online: July 14, 2022